

A luminous and young galaxy at $z = 12.33$ revealed by a JWST/MIRI detection of $H\alpha$ and [OIII]

Jorge A. Zavala¹, Marco Castellano², Hollis B. Akins³, Tom J. L. C. Bakx⁴, Denis Burgarella⁵, Caitlin M. Casey³, Óscar A. Chávez Ortiz³, Mark Dickinson⁶, Steven L. Finkelstein³, Ikki Mitsuhashi^{1,7}, Kimihiko Nakajima¹, Pablo G. Pérez-González⁸, Pablo Arrabal Haro⁶, Pietro Bergamini^{9,10}, Veronique Buat⁵, Bren Backhaus¹¹, Antonello Calabrò², Nikko J. Cleri^{12,13}, David Fernández-Arenas^{14,15}, Adriano Fontana², Maximilien Franco³, Claudio Grillo^{9,16}, Mauro Giavalisco¹⁷, Norman A. Grogin¹⁸, Nimish Hathi¹⁸, Michaela Hirschmann^{19,20}, Ryota Ikeda^{1,21}, Intae Jung¹⁸, Jeyhan S. Kartaltepe²², Anton M. Koekemoer¹⁸, Rebeca L. Larson^{3,22}, Jed McKinney³, Casey Papovich^{12,13}, Piero Rosati^{23,10}, Toshiaki Saito¹, Paola Santini², Roberto Terlevich^{24,25,26}, Elena Terlevich^{24,26}, Tommaso Treu²⁷, and L. Y. Aaron Yung¹⁸

(Affiliations are included at the end of the document)

The James Webb Space Telescope (JWST) has discovered a surprising population of bright galaxies in the very early universe ($\lesssim 500$ Myrs after the Big Bang) that is hard to explain with conventional galaxy formation models and whose physical properties remain to be fully understood. Insight into their internal physics is best captured through nebular lines but, at these early epochs, the brightest of these spectral features are redshifted into the mid-infrared and remain elusive. Using the JWST Mid-Infrared Instrument, MIRI, here we present the first detection of $H\alpha$ and doubly-ionized oxygen ([OIII]4959,5007 Å) at $z > 10$. These detections place the bright galaxy GHZ2/GLASS-z12 at $z = 12.33 \pm 0.04$, making it the most distant astronomical object with direct spectroscopic detection of these lines. These observations provide key insights into the conditions of this primeval, luminous galaxy, which shows hard ionizing conditions rarely seen in the local Universe likely driven by compact and young ($\lesssim 30$ Myr) burst of star formation. Its oxygen-to-hydrogen abundance is close to a tenth of the solar value, indicating a rapid metal enrichment. This study confirms the unique conditions of this remarkably bright and distant galaxy and the huge potential of mid-IR observations to characterize these objects.

Following the confirmation of the first surprisingly bright galaxies at high-redshifts ($z \gtrsim 10$)^{1–3}, research efforts must now shift towards gaining a deeper understanding of their physical properties. The detection and interpretation of emission-line spectra are pivotal in this topic, with well-studied calibrations and diagnostic diagrams based on rest-frame optical transitions and line ratios such as [NII]/ $H\alpha$ vs [OIII]/ $H\beta$. The advent of the JWST and, particularly, the

sensitive Near Infrared Spectrograph (NIRSpec), has now unlocked access to some of these lines in very high-redshift galaxies, enabling detailed studies that were previously unreachable beyond $z \sim 3$ (e.g.^{4,5}). At redshifts above $z \sim 7$, however, the $H\alpha$ transition, known as the gold standard to measure young star formation activity, is redshifted beyond the NIRSpec coverage. Similarly, the [OIII] and $H\beta$ lines, sensitive to metallicity and ionizing conditions, can only be observed up to $z \sim 9.5$ with this instrument.

The MIRI instrument on board JWST is thus the only astronomical instrument with the required wavelength coverage to detect these spectral lines at higher redshifts, critical for characterizing the physical properties of the first galaxies in the universe. While early predictions suggested that their successful detection may require long observing times of several tens of hours⁶, the combination of both the better-than-expected performance of JWST⁷ and the remarkably high brightness of some of the JWST-discovered distant galaxies, might have improved the prospects for such studies, making the detection of $z > 10$ rest-frame optical emission lines more feasible than previously anticipated.

Here, we report the results of the first MIRI spectroscopic observations on a $z > 10$ galaxy candidate and test its efficiency for redshift confirmation and characterization of early galaxies via the detection of rest-frame optical nebular lines.

We target the galaxy GHZ2/GLASS-z12^{8,9} (RA = $00^{\text{h}}13^{\text{m}}59.76^{\text{s}}$, DEC = $-30^{\circ}19'29.11''$) with MIRI to search for the brightest rest-frame optical nebular emission lines redshifted into the mid-IR regime: [OIII]4959,5007 Å, $H\alpha$, $H\beta$ (with the doublets [NII]6548,6583 Å and [SII]6716,6731 Å also covered but expected to be too faint to be detected). The target stands out as one of the brightest and most robust among the extremely distant galaxy candidates found in deep JWST NIRCам images, with a photometric redshift of $z \approx 12.0 - 12.4$. It was found in the outskirts of the galaxy cluster Abell 2744, as part of the GLASS-JWST Early Release Science Program¹⁰, with an absolute rest-frame UV magnitude of $M_{\text{UV}} = -20.5$ mag¹¹ and a inferred stellar mass⁹ close to $10^9 M_{\odot}$, despite its compact morphology¹² ($R_e \lesssim 50$ pc) and moderate gravitational amplification of¹³ $\mu \approx 1.3$ (see Methods for a deeper discussion on the gravitational amplification).

The MIRI observations were conducted on October 25–29, 2023, using the low resolution spectrometer (LRS) slit mode (resolving power $R \approx 50 - 200$), with a total integration on-source exposure time of 9 h (see details in the

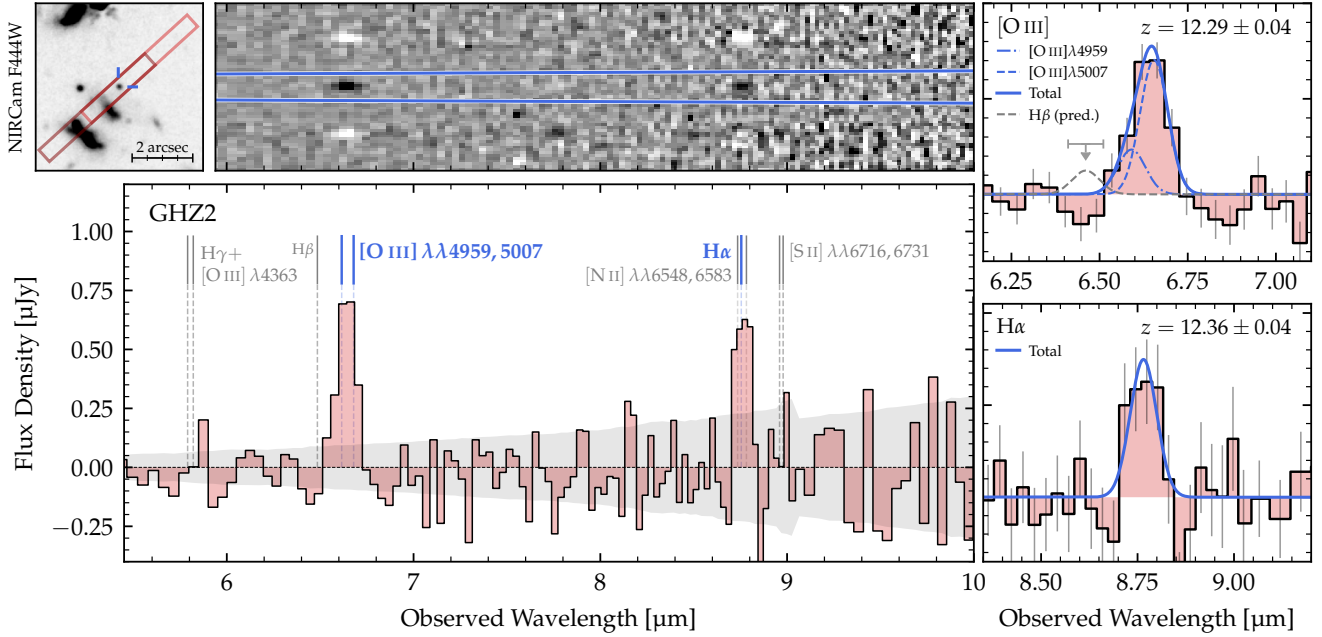


Figure 1: **JWST/MIRI spectrum of GHZ2 at $z = 12.33$.** **Top left:** NIRCам F444W cutout image ($5'' \times 5''$) centered at the position of GHZ2, with the MIRI/LRS slit illustrated with the red rectangle (at the two different dither positions). The combined 2D spectrum and the used aperture for the 1D extraction are also plotted (see details in the Section Methods). **Bottom left:** 1D extracted spectrum at the position of GHZ2 across the most sensitive wavelength range, $\lambda_{\text{obs}} \approx 5.7 - 10 \mu\text{m}$ and the associated 1σ uncertainty (gray region). The expected wavelengths of typically bright rest-frame optical emission lines are indicated with the vertical lines, with the blue text highlighting the robust detections. **Right:** Zoom-in on the detected spectral features identified as the [OIII]4959,5007Å doublet (*top*) and the H α emission line (*bottom*) along with the best-fit Gaussian functions and the implied redshifts and associated 1σ uncertainties, which are dominated by the current wavelength calibration. In the top panel, the 2.5σ upper limit for the H β line is indicated with the downward arrow, while the predicted H β line from the Balmer decrement (assuming a dust-free scenario) is represented by the gray dashed line.

Methods). The main advantage of this mode relies on its large spectral coverage, which provides sensitive observations across $\approx 5-12 \mu\text{m}$, covering at least one of the aforementioned lines across $z \approx 7 - 20$. Data reduction was performed using the standard JWST pipeline with some additional steps as described in the Methods.

Fig. 1 shows the MIRI one-dimensional (1D) and two-dimensional (2D) spectra of the source. Two spectroscopic features are clearly detected above the noise level ($> 5\sigma$) in the 1D and 2D spectra. These spectral features are associated with the [OIII] doublet (4959Å and 5007Å) and with the H α recombination line, which constrain the redshift of this source to be $z_{\text{spec}} = 12.33 \pm 0.04$ (see also ref.¹¹), making this object the most distant galaxy with detections of these nebular lines and one of the brightest early galaxies discovered to date. The JWST/NIRSpec spectra of the other five galaxies with similar spectroscopic redshifts¹⁴⁻¹⁷ ($z \approx 12 - 14$) are distinguished by the lack of strong emission lines. In these cases, the spectroscopic redshifts are measured via the spectral break in continuum emission produced by absorption of neutral hydrogen, but extensive tests are needed to rule out lower-redshift solutions that can produce similar breaks. This demonstrates the unique use

of MIRI to spectroscopically confirm the highest redshift galaxies via direct detection of rest-frame optical lines that can additionally provide direct information on the galaxy's star formation rate and ionized gas properties, although these studies might be limited to the brightest systems.

The emission line around $6.6 \mu\text{m}$, associated with the [OIII] doublet, was fitted with a double Gaussian function to infer the line flux densities (reported in Table 1). During this procedure we assume the same line-width for the two lines and fix the relative intensity ratio to the theoretical 1:3 value¹⁸. In the case of H α , the line was fitted with a single Gaussian function. Although the [NII] doublet lines are blended with H α , at the redshift of GHZ2, it is reasonable to assume that the flux contribution of [NII] is negligible due to the likely sub-solar metallicity^{19,20}. Negligible [NII] emission is seen even at lower redshifts ($z \approx 4 - 7$) for galaxies^{5,21-23} and AGN alike^{24,25}, an even for nitrogen-enriched systems²³. Hence, we can safely assume that this line is dominated by the H α emission. For the undetected emission lines, including H β and the [SII] doublet, 2.5σ upper limits were derived by adopting the local noise r.m.s and a given line-width as described in the Methods. Note that the non-detection of H β is still consistent with theo-

retical predictions and with zero dust attenuation. A more stringent upper limit on the $H\beta$ flux density can be inferred from the measured $H\alpha$ flux density, adopting a flux ratio of $H\alpha/H\beta = 2.85$ (based on the so-called case-B recombination scenario and under the typical physical conditions of galaxies’ ionized gas²⁶). This ratio is valid in the case of negligible dust attenuation, but it increases in the presence of dust since the $H\beta$ line is more affected by dust extinction. Nevertheless, the dust attenuation is not expected to be significant in this galaxy (with inferred A_V values around or below 0.1-0.3 mag, as described in the Methods).

This record-breaking detection of $H\alpha$ provides a direct probe of the young star formation activity, tracing massive stars with ages around or below 10 Myr. This, combined with the detection of oxygen (revealing the presence of metals and thus of more evolved stars), provides a unique opportunity to study the stellar population of this distant galaxy and its ionizing photon production efficiency. We infer the average stellar age, and other properties like stellar mass and star formation rate, by conducting spectral energy distribution (SED) fitting to the NIRCcam photometry jointly with the constraints from the $H\alpha$ and [OIII] emission lines (see details in the Methods and Supplementary materials). The photometry and the spectroscopic data are well reproduced with a model with a composite star formation history extending for ~ 50 Myr, with a mass-weighted age of 28^{+10}_{-14} Myr, and more than 60% of the total stellar mass formed during the past 30 Myr. The presence of young and massive stars implies a higher rate of ionizing photon production compared to typical values in galaxies at lower redshifts (see Figure 4). The evidence that most of the stellar mass of GHZ2 formed recently is consistent with other results implying that early galaxies have more “bursty” star-formation histories^{31–34}). If the majority of early galaxies do indeed form the bulk of their visible mass in their recent past, it could explain not only the remarkable luminosity of this distant galaxy, but the overall surprising number of observed bright galaxies in this epoch^{35,36}.

The SED-based SFR (averaged on the last 10 Myr and taking into account the gravitational lensing amplification of¹³ $\mu = 1.3$) of $5 \pm 2 M_\odot \text{ yr}^{-1}$ is in good agreement with the SFR of $9 \pm 3 M_\odot \text{ yr}^{-1}$ estimated directly from the $H\alpha$ luminosity assuming the calibration from ref.³⁷. This calibration is based on low-metallicity stellar population synthesis models that include the effects of massive stars in binary systems characterized by a high ionizing photon production efficiency. On the other hand, the widely-adopted calibration used for local and low-redshift galaxies³⁸ predicts a higher SFR of $\sim 22 \pm 5 M_\odot \text{ yr}^{-1}$, mainly due to the absence of these low-metallicity and binary stars.

The JWST/MIRI data also constrain the $R3 \equiv \log([OIII]/H\beta)$ ratio, which is known to correlate with the

gas-phase metallicity³⁹. The estimated line ratio and its associated uncertainty of $[OIII]/H\beta = 5.2 \pm 1.5$ (when assuming directly the inferred $H\beta$ in the case of zero dust attenuation) implies a metallicity of $12 + \log(O/H) = 7.40^{+0.52}_{-0.37}$ according to the relation presented by ref.⁴⁰, corresponding to $Z = 0.05^{+0.12}_{-0.03} Z_\odot$ (where Z_\odot is solar metallicity). A similar range of metallicities are obtained when using the theoretical calibrations⁴¹ specifically designed for galaxies at $z > 4$ (see details in the Methods). These values are in good agreement with the independent metallicity estimation of $12 + \log(O/H) = 7.26^{+0.27}_{-0.24}$ based on the $[NeIII]3868\text{\AA}/[OII]3727\text{\AA}$ index (with additional constraints from other lines), as reported in our parallel analysis of the NIRSpc data of this source¹¹.

Despite the young age derived for GHZ2, it is notable that its metallicity is already enriched to a few percent (or even up to $\sim 10 - 15\%$) of the solar value, significantly above expectations for the primordial objects dominated by the first-generation stars (typically known as population-III stars). This implies a very rapid metal enrichment during the earliest phases of galaxy formation. The metallicity inferred for GHZ2 is higher than the metallicities of the four spectroscopically-confirmed galaxies at $z = 10 - 13$ discovered in the JADES survey¹⁴. This is not totally surprising since a correlation between stellar mass and metallicity is known to exist even up to $z \sim 9$ ²⁷, and the stellar mass of GHZ2 of $\log(M_\star/M_\odot) \approx 8.6 - 9.0$ is around an order of magnitude larger than what was inferred for JADES galaxies. This might suggest that a similar relation exists even at these early redshifts, although shifted to lower metallicities. Actually, when compared with the so-called fundamental metallicity relation⁴², which involves the SFR as a third parameter, all these $z > 10$ galaxies deviate significantly towards lower metallicity values. Confirming the existence of such scaling relations would require, however, larger samples of galaxies with similar spectroscopy data.

To gain further insights into the physical conditions of the ionized gas in this galaxy, we show in Fig. 2 the well-studied $[NII]/H\alpha$ vs $[OIII]/H\beta$ BPT-diagram along with the predictions from a photoionization model powered by star formation⁴⁴. The $R3$ value of 5.2 ± 1.5 derived above implies a high ionization parameter of $\log(U) \gtrsim -2.0$, as shown in Fig. 2. Note that this measurement is not affected by our assumption of a dust-free environment when calculating the $H\beta$ line since any dust attenuation will only increase the inferred $[OIII]/H\beta$ ratio. The high ionization conditions in this galaxy are also confirmed by the detection of $[NIV]1488\text{\AA}$ and $HeII 1640\text{\AA}$ in the NIRSpc spectrum¹¹, requiring ionizing photons with energy above ~ 54 eV. This might point towards the presence of X-ray binaries or very massive stars^{45–47} contributing to the hard ionizing radiation.

Alternatively, the high ionization conditions might be

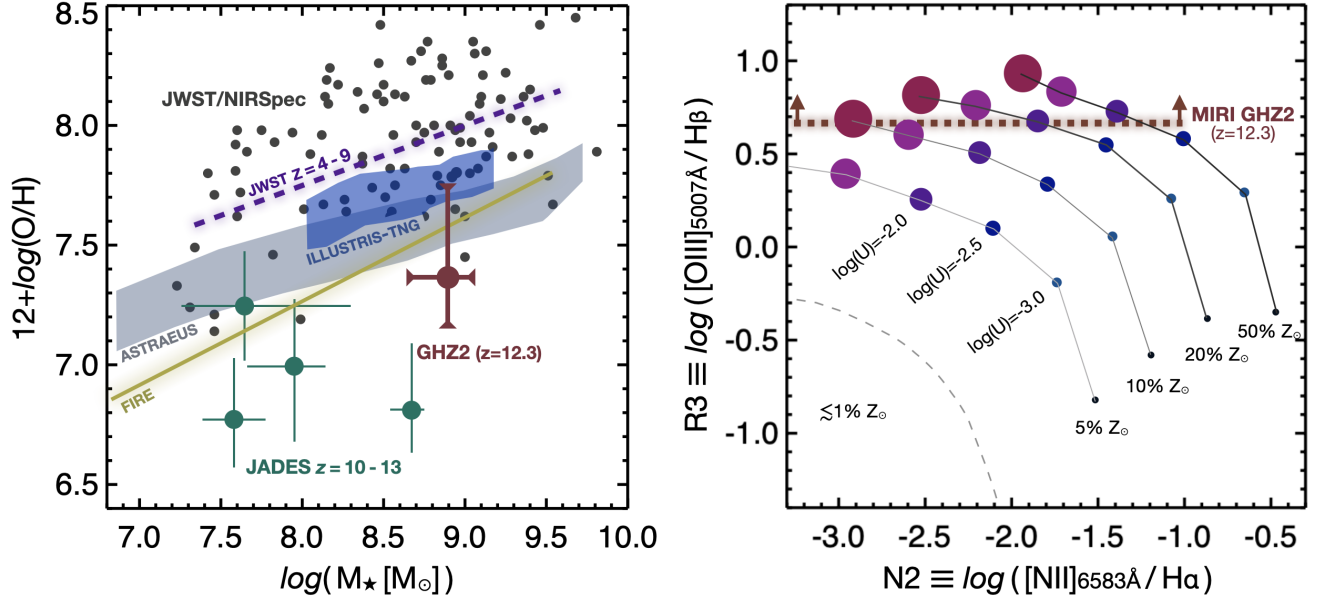


Figure 2: The stellar mass-metallicity relation and the ionization diagnostic diagram. **Left:** Position of GHZ2 in the stellar mass-metallicity plane in comparison to lower redshift galaxies at $z \approx 4 - 9$ (black dots for individual galaxies and purple line for best-fit relationship²⁷) and with the $z = 10 - 13$ galaxies from the JADES survey¹⁴ (green points; metallicity estimated from SED fitting). Error bars represent 1σ uncertainties in the stellar mass values and the range of allowed values for the metallicities. All the $z > 10$ galaxies, including GHZ2, are off from the lower-redshift relationship²⁷, suggesting an evolution towards lower metallicity values at earlier epochs. The predictions from the FIRE²⁸ (golden line) and ASTRAEUS²⁹ (gray region) simulations at $z \sim 10$ show a broad agreement with the current constraints, while the ILLUSTRIS-TNG³⁰ simulations (blue region) predict slightly higher metallicities, although still consistent within the error bars. Despite the early epochs, none of these galaxies show pristine (close-to-zero) metallicities, implying a rapid metal enrichment in the early Universe. **Right:** The $[\text{NII}]/\text{H}\alpha$ vs $[\text{OIII}]/\text{H}\beta$ diagram along with the predictions from a stellar photoionization model²⁰ assuming four different metallicities and six ionization parameters in steps of 0.5dex (models with $Z \lesssim 0.01 Z_{\odot}$ would lie below the dashed line). The observational constraints on the R3 value (formally a lower limit derived under the assumption of zero dust attenuation) implies high ionizing conditions, with $\log(U) > -2.0$.

produced by AGN activity, although the higher ionization AGN tracers $\text{NeIV}]2424\text{\AA}$ and $[\text{NeV}]3426\text{\AA}$ remain undetected¹¹. On the other hand, a morphological analysis of this object constrains its size to be very compact ($r_e \lesssim 50$ pc) but marginally resolved¹², which favors the star-formation scenario as the source of the ionizing radiation or a composite AGN/star-forming galaxy system (rather than pure AGN).

It is now useful to put into context the upper limit on the $[\text{OIII}]88\mu\text{m}$ line luminosity derived from previous ALMA observations⁴⁸. The line ratio between this and the $[\text{OIII}]5007\text{\AA}$ transition is sensitive to the electron density of the ionized gas with an extra milder dependency on temperature. Fig. 3 shows the expected $[\text{OIII}]5007\text{\AA}$ -to- $[\text{OIII}]88\mu\text{m}$ line ratio as a function of electron temperature and density (see Methods section for further details). As can be seen, at the typical $[\text{OIII}]$ electron temperatures (e.g. 6,000-15,000 K), the constraints imposed by the ALMA and JWST observations imply a high electron density above 10^3 cm^{-3} . This, again, contrasts with the typical conditions seen in the local Universe and lower redshift galaxies with average densities on the order of⁴³ $n_e \approx 10^1 - 10^2 \text{ cm}^{-3}$, but is in agreement with the recent results proving a redshift evo-

lution towards higher electron densities at high redshifts⁴⁹ (see also Figure 5). This evolution might be driven by the higher star formation rate surface density (Σ_{SFR}) measured in high-redshift galaxies^{22,23,50}, which reaches an extreme value of $320 \pm 130 M_{\odot} \text{ yr}^{-1} \text{ kpc}^{-2}$ in GHZ2 (adopting the measured¹² effective radius of 50 pc). The combination of these unique conditions, including high ionization parameters, high electron densities, and high star formation rate surface density might explain the brightness of the unique population of $z > 10$ galaxies recently discovered by JWST, along with the young stellar ages and relatively low metallicities.

This study demonstrates the enormous potential of the Mid-Infrared Instrument, MIRI, on board JWST for the confirmation and characterization of the most distant galaxies in the Universe. Our observations make our target, GHZ2, the most distant galaxy with direct detection of several transitions from the ionized gas (see also ref.¹¹) and one of the brightest spectroscopically-confirmed galaxy at this early epoch, with a robust spectroscopic redshift of $z = 12.33 \pm 0.04$. The physical conditions of GHZ2, revealed directly by nebular emission lines, are extreme

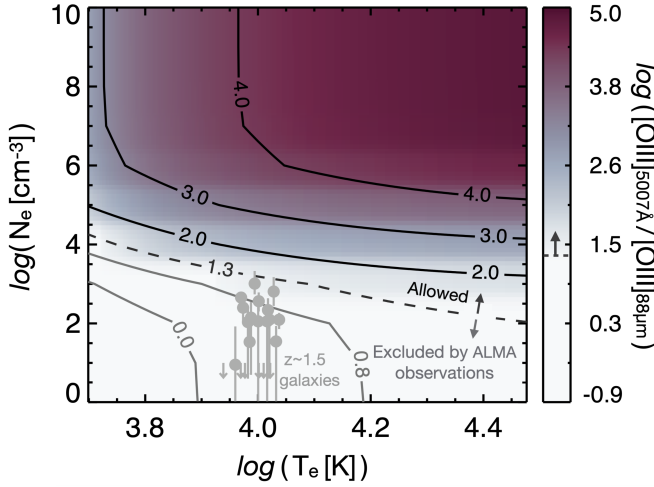


Figure 3: **Electron density constraints.** Predicted [OIII]5007Å-to-[OIII]88μm line ratio (illustrated in different colors and enclosed by the contours) as a function of electron density (n_e ; y-axis) and electron temperature (T_e ; x-axis). The constraints from the available ALMA observations in combination with the JWST/MIRI data, with $\log([OIII]_{5007A}/[OIII]_{88\mu m}) \gtrsim 1.3$, imply high electron densities above even above $1,000 \text{ cm}^{-3}$ at the typically adopted electron temperature of $T_e = 10,000 \text{ K}$ (with a minimum electron density of 100 cm^{-3} , depending on T_e). This is higher than the typical values measured at lower redshifts, corroborating the extreme conditions of this early galaxy. For comparison, we plot the estimated electron densities (and associated 1σ uncertainties) for a sample of $z \sim 1.5$ galaxies with direct n_e measurements from the [OII] doublet⁴³ (T_e were scattered around the adopted $10,000 \text{ K}$ for better visualization).

and rarely seen in the local Universe, with a low (but not pristine) metallicity, high ionization conditions, and high electron density. This emerging picture of compact galaxies with extreme conditions seems to be fairly common at high redshifts, particularly among the brightest systems, and might be associated with short bursts of young star formation with ages of a few tens of Myr and with the presence of massive, low-metallicity stars. Some of the properties of this early galaxy might also resemble the observed features of AGN, particularly the hard ionizing spectra inferred from the observations presented here and from the JWST/NIRSpec data¹¹. It is thus possible that this source might be, at least partially, powered by an active black hole. Further observations on this and other similar sources will significantly contribute to our understanding of early galaxy formation and black-hole growth, pushing the current frontiers into the formation epoch of the first massive objects in the Universe.

Data availability. The JWST/MIRI data used in this paper will be publicly available through the Mikulski Archive for Space Telescopes server, under JWST program GO-3703. All other data generated throughout the analysis are

available from the corresponding author, JAZ, on request.

Acknowledgements. This work is based on observations made with the NASA/ESA/CSA James Webb Space Telescope. The data were obtained from the Mikulski Archive for Space Telescopes at the Space Telescope Science Institute, which is operated by the Association of Universities for Research in Astronomy, Inc., under NASA contract NAS 5-03127 for JWST. These observations are associated with program JWST-ERS-3703. This paper makes use of the following ALMA data: ADS/JAO.ALMA#2021.A.00020.S. ALMA is a partnership of ESO (representing its member states), NSF (USA), and NINS (Japan), together with NRC (Canada), MOST, ASIAA (Taiwan), and KASI (Republic of Korea), in cooperation with the Republic of Chile. The Joint ALMA Observatory is operated by ESO, AUI/NRAO, and NAOJ. JAZ acknowledge funding from JSPS KAKENHI grant number KG23K13150. The GLASS-JWST team and other co-authors acknowledges support by NASA via grants JWST-ERS-1342 and JWST-GO-3703. C.G. acknowledges financial support through grant PRIN-MUR 2020SKSTHZ. Finally, we would like to thank Sarah Kendrew, Greg Sloan, and Milo Docher for their support during the preparation of the observations and their suggestions for data reduction.

Author Contributions. J.A.Z. led the JWST MIRI observing proposal, data analysis, and manuscript writing. M.C., A.C., A.F., P.S. and T.T. led the original JWST GLASS observations and the discovery study of GHz2, and contributed to the MIRI follow-up proposal. H.B.A and J.M. significantly contributed to the MIRI data reduction. T.J.L.C.B. and I.M. re-analyzed the ALMA data and the [OIII]88μm constraints. D.B., O.A.C.O., S.L.F., P.P.G., V.B. and P.S. modelled and interpreted the spectral energy distributions of our target. P.B., C.G., and P.R. performed the lensing analysis presented in the Methods. M.D., C.M.C., P.A.H., M.F., M.G., N.A.G., N.H., R.I., I.J., J.S.K., A.M.K., R.L.L. and C.P., contributed to the original JWST MIRI proposal, observing design, and to the scientific discussion in the proposal and manuscript. M.C., K.N., A.C., B.B., N.J.C., D.F.A., C.P., R.T., E.T. and T.S. focused on the interpretation of the observed lines and line ratios (and associated derived physical properties). K.N., M.H. and L.Y.A.Y. provided the theoretical grounds to infer some of the physical parameters and other predictions from simulations. All co-authors contributed to the editing and formatting of the manuscript.

Competing interests. The authors declare no competing interests.

Affiliations

¹National Astronomical Observatory of Japan, 2-21-1, Osawa, Mitaka, Tokyo, Japan

²INAF - Osservatorio Astronomico di Roma, Via Frascati 33, 00078, Monte Porzio Catone, Italy

³Department of Astronomy, The University of Texas at Austin, 2515 Speedway Boulevard Stop C1400, Austin, TX 78712, USA

⁴Department of Space, Earth, & Environment, Chalmers University of Technology, Chalmersplatsen 4, SE-412 96 Gothenburg, Sweden

⁵Aix Marseille Univ, CNRS, CNES, LAM, Marseille, France

⁶NSF's National Optical-Infrared Astronomy Research Laboratory, 950 N. Cherry Avenue, Tucson, AZ 85719, USA

⁷Department of Astronomy, The University of Tokyo, 7-3-1 Hongo, Bunkyo, Tokyo 113-0033, Japan

⁸Centro de Astrobiología (CAB), CSIC-INTA, Ctra. de Ajalvir km 4, Torrejón de Ardoz, E-28850, Madrid, Spain

⁹Dipartimento di Fisica, Università degli Studi di Milano, Via Celoria 16, I-20133 Milano, Italy

¹⁰INAF – OAS, Osservatorio di Astrofisica e Scienza dello Spazio di Bologna, via Gobetti 93/3, I-40129 Bologna, Italy

¹¹Department of Physics, 196A Auditorium Road, Unit 3046, University of Connecticut, Storrs, CT 06269, USA

¹²Department of Physics and Astronomy, Texas A&M University, College Station, TX 77843-4242 USA

¹³George P. and Cynthia Woods Mitchell Institute for Fundamental Physics and Astronomy, Texas A&M University, College Station, TX 77843-4242 USA

¹⁴Canada-France-Hawaii Telescope, Kamuela, HI 96743, USA

¹⁵Instituto de Radioastronomía y Astrofísica, UNAM Campus Morelia, Apartado postal 3-72, 58090 Morelia, Michoacán, Mexico

¹⁶INAF – IASF Milano, via A. Corti 12, I-20133 Milano, Italy

¹⁷University of Massachusetts Amherst, 710 North Pleasant Street, Amherst, MA, 01003-9305, USA

¹⁸Space Telescope Science Institute, 3700 San Martin Dr, Baltimore, MD 21218, USA

¹⁹Institute for Physics, Laboratory for Galaxy Evolution and Spectral Modelling, Ecole Polytechnique Federale de Lausanne, Observatoire de Sauverny, Chemin Pegasi 51, 1290 Versoix, Switzerland

²⁰INAF, Osservatorio Astronomico di Trieste, Via Tiepolo 11, I-34131 Trieste, Italy

²¹Department of Astronomy, School of Science, SOKENDAI (The Graduate University for Advanced Studies), 2-21-1 Osawa, Mitaka, Tokyo 181-8588, Japan

²²Laboratory for Multiwavelength Astrophysics, School of Physics and Astronomy, Rochester Institute of Technology, 84 Lomb Memorial Drive, Rochester, NY 14623, USA

²³Dipartimento di Fisica e Scienze della Terra, Università degli Studi di Ferrara, via Saragat 1, I-44122 Ferrara, Italy

²⁴Instituto Nacional de Astrofísica, Óptica y Electrónica, Tonantzintla, 72840 Puebla, Mexico

²⁵Institute of Astronomy, University of Cambridge, Cambridge CB3 0HA, UK

²⁶Facultad de Astronomía y Geofísica, Universidad de La Plata,

Paseo del Bosque s/n, B1900FWA La Plata, Argentina

²⁷Department of Physics and Astronomy, University of California, Los Angeles, 430 Portola Plaza, Los Angeles, CA 90095, USA

Methods

1 Cosmology and other definitions

Throughout this paper, we assume a flat Λ CDM cosmology with $\Omega_m = 0.29$, $\Omega_\Lambda = 0.71$ and $H_0 = 69.6 \text{ km s}^{-1} \text{ Mpc}^{-1}$; and a Solar abundance of 12 + $\log(\text{O}/\text{H}) = 8.69$ ⁵¹.

2 JWST/MIRI observations and data reduction

Observations were conducted as part of project GO-3703 (PI: J. Zavala) using the MIRI low resolution spectrometer (with the P750L filter) in slit mode. The target was observed in three different visits using the FASTR1 readout pattern and 121 groups per integration, 16 integration per exposure, and 1 exposure per specification with 2 dither positions "along slit nod". Each visit has an on-source time of 10828.26 s (summing 9 h in total). Target acquisition (TA) observations on a bright star (RA=00h13m58.3s; Dec=-30°20'14.10") were conducted before every visit to ensure the target is placed with subpixel accuracy ($< 10 \text{ mas}$) at the nominal slit center location.

We reduce the MIRI data using the official *JWST* pipeline (Version 1.13.4), Calibration Reference Data System (CRDS) version 11.16.16 and CRDS context `jwst_1174.pmap` to assign the reference files. We adopt the stage 1 pipeline procedures unchanged, resulting in six count-rate images (2 dithers, 3 exposures each). Then, we run the `spec2pipeline` stage, which performs flux calibration and various instrument corrections, separately on the individual count-rate exposures, yielding six individual `s2d` images. Due to the presence of a bright nearby galaxy within the slit in one of the dither positions (see the top-left panel in Fig. 1), some residual emission is seen in half of the data. Therefore, we continue to treat each dither position separately, averaging the three exposures for each first and yielding one `s2d` file for each dither. Next, we perform a background subtraction on each dither, separately, rather than simply subtracting the two. This was done using the `Background2D` task in `photutils`, masking a $r = 3.5$ pixel circular region around the detected emission lines. We estimate the median background using a box size of 2×2 pixels. We then input these background-subtracted `s2d` files into the `spec3pipeline` stage, which performs outlier rejection via sigma clipping and combines the two dither positions into a single 2D spectrum. Finally, we perform 1D extraction manually using a boxcar filter with a width that scales with the MIRI PSF FWHM, as shown in the top panel of Fig. 1. Above $9 \mu\text{m}$, where the noise r.m.s. per channel notably increases (due to the sensitivity of the detector and the higher spectral resolution), we re-bin the data with a 2-channel bin.

An alternative reduction following the standard steps in

the pipeline, results in a similar spectrum but with a continuum baseline slightly offset towards negative values. After correcting this systematic offset, the [OIII] line luminosity is around 20% brighter than in our manual reduction, but with lower signal-to-noise ratio. Given that our modified reduction provides better r.m.s. noise across the whole spectrum, we adopt it for our analysis, but note that our results would not significantly change otherwise.

3 Spectroscopic redshift and line measurements

Emission line fitting and line ratios: A single Gaussian function was used to fit the $\text{H}\alpha$ line assuming negligible contribution from the [NII] doublet. In the case of the [OIII] doublet, we perform a simultaneous two-Gaussian fitting. During this procedure we assume the same line-width for the two lines (leaving it as a free parameter) and fix the 5007/4959 peak line ratio to 3. We use a Levenberg-Marquardt algorithm to perform non-linear least-square minimization (using the `LMFIT` function). The measured line-widths are consistent with the instrumental resolution⁵² of $R \equiv \Delta\lambda/\lambda \approx 81$ around the position of the [OIII] doublet (vs $R \approx 83$ from the measured line-width) and 132 around $\text{H}\alpha$ (with a slightly wider measured line-width corresponding to $R \approx 103$).

To infer an upper limit on the $\text{H}\beta$ line flux density, we assume the 2.5σ r.m.s value as the upper limit for the line peak and the same line-width as the [OIII]5007Å line, which is determined by the line spread function of the instrument. This is a reasonable assumption since the lines are very close in wavelength space and thus the spectral resolution is expected to be very similar. This results in a $\text{H}\beta$ line flux upper limit of $2.0 \times 10^{-18} \text{ erg s}^{-1} \text{ cm}^{-2}$. Alternatively, the $\text{H}\beta$ line flux density was inferred from the detected $\text{H}\alpha$ line. In the case of a dust-free environment and Case B recombination-line radiation (see details in ref.²⁶), the expected $\text{H}\alpha$ -to- $\text{H}\beta$ line ratio is 2.85 for $n_e = 10^4 \text{ cm}^{-3}$ and $T_e = 10,000 \text{ K}$ (note that this ratio does not change significantly for other values of density and temperature). Under these assumptions, we estimate an integrated line flux density of $0.9 \times 10^{-18} \text{ erg s}^{-1} \text{ cm}^{-2}$. We adopt this value along the paper since we do not expect a significant dust attenuation for this galaxy (based on the SED fitting results, the dust continuum ALMA constraints⁴⁸, and the blue UV slope¹¹). Actually, adopting the Calzetti attenuation law⁵³ and dust extinction values of $A_V \approx 0.1 - 0.3$ – similar to the SED fitting results described below – would decrease the estimated $\text{H}\beta$ line flux only by $\lesssim 10\%$.

Finally, a 2.5σ upper limit for the [SII] doublet was derived using the local r.m.s value around $8.97 \mu\text{m}$ and adopting a line-width 5% narrower than the $\text{H}\alpha$ line (following the expected spectral response of the instrument⁵²). All these measurements are reported in Table 1.

Spectroscopic redshift. The dominant uncertainty on the spectroscopic redshift comes from the current MIRI/LRS wavelength calibration. While the current calibration accuracy is estimated to be around ± 20 nm¹, this still can introduce a redshift offset of $\Delta z \sim 0.04$. A recent calibration update (referenced as `jwst_1174.pmap` in the JWST pipeline), introduced a shift of about 50 nm at 6 microns and decreasing to nearly zero at the red end of the spectral range. A similar correction but a bit less extreme in the blue part was independently found by ref.⁵⁴ using observations of a Y Dwarf. Fitting the line with a single Gaussian component, we obtain $z_{H\alpha} = 12.36 \pm 0.02$ (random) ± 0.04 (systematic) with the updated 2024 JWST calibration. For comparison, adopting the calibration from ref.⁵⁴, we obtain $z_{H\alpha} = 12.37 \pm 0.02$ (random) ± 0.04 (systematic). In the case of the [OIII] doublet, and using a two-Gaussian simultaneous fitting as described above, we obtain $z_{[\text{OIII}]}$ = 12.29 ± 0.01 (random) ± 0.04 (systematic) using the most recent pipeline calibration, or $z_{[\text{OIII}]}$ = 12.33 ± 0.01 (random) ± 0.04 (systematic) using an alternative wavelength calibration⁵⁴. The differences between the inferred redshifts are mainly attributed to the current wavelength calibration uncertainty of ~ 20 nm. Across this paper we adopted the average of the redshifts obtained with the official pipeline calibration, resulting in $z = 12.33 \pm 0.02$ (random) ± 0.04 (systematic) (or simply $z = 12.33 \pm 0.04$, after taking the square root of the sum of the square of the two errors). Similar redshift constraints were derived from the NIRSpec observations¹¹ with a weighted redshift average between four different emission lines of $z = 12.342 \pm 0.009$. A more precise MIRI/LRS wavelength calibration in the future will allow to derive spectroscopic redshifts with better than 1 % precision even with the low resolution spectrometer.

4 Inferred parameters from the emission lines.

Metallicity: We adopted the recent calibration from ref.⁴⁰ based on a sample of 46 galaxies at $z \approx 2 - 9$ observed with JWST/NIRSpec and with multiple line detections (including temperature-sensitive lines), from which we derive $12 + \log(\text{O}/\text{H}) = 7.40^{+0.52}_{-0.37}$ taking into account the uncertainty on the [OIII]-to- $H\beta$ line ratio and the observed scatter in the calibration sample. This corresponds to $Z = 0.05^{+0.12}_{-0.03} Z_{\odot}$. Using instead the calibration from ref.⁴⁴, calibrated using local analogs, results in a consistent metallicity of $\sim 0.1 Z_{\odot}$. We finally use the theoretical predictions for metallicity calibrations of ref.⁴¹, based on the IllustrisTNG⁵⁵ simulations connected to photo-ionisation models and focused only on galaxies at $z > 4$. This theoretical calibration implies a metallicity of $Z = 0.04 \pm 0.02 Z_{\odot}$.

Note that our assumption of a negligible dust attenuation when estimating the $H\beta$ line luminosity does not bias the inferred metallicity. This is due to the turnover of the relation at higher metallicities where lower values of [OIII]-to- $H\beta$ are expected (while dust attenuation would imply higher line ratios). This turnover implies, however, a second solution for GHZ2 of $Z \approx 0.55 Z_{\odot}$. This value is inconsistent with the independent constraints obtained from the NIRSpec data¹¹, with several diagnostic suggesting values around or below $0.1 Z_{\odot}$. We can thus conclude that the gas-phase metallicity in GHZ2 is close to the aforementioned value of $Z = 0.05^{+0.12}_{-0.03} Z_{\odot}$; relatively low compared to lower redshift galaxies, but not pristine despite its young age.

Balmer decrement: In the presence of dust, the $H\alpha$ -to- $H\beta$ line ratio is expected to deviate from the theoretical value since the short-wavelength $H\beta$ transition is more susceptible to dust attenuation. However, while the upper limit on the $H\beta$ line luminosity is consistent with a dust-free scenario it does not rule out the possibility of dust attenuation. Deeper observations will be necessary to put any constraints on the presence (or absence) of dust in this galaxy via the Balmer decrement.

SFR and ionizing photon production efficiency. As mentioned in the main text, we estimate a SFR of $12 \pm 4 M_{\odot} \text{ yr}^{-1}$ (or $9 \pm 3 M_{\odot} \text{ yr}^{-1}$ after taking into account the gravitational magnification of $\mu = 1.3$ estimated by ref.¹³) using the calibration³⁷ $\text{SFR}/L(\text{H}\alpha) = 10^{-41.67} (M_{\odot} \text{ yr}^{-1}) / (\text{erg s}^{-1})$. This calibration was derived from $Z = 0.001$ BPASS population synthesis models with an upper-mass IMF cut of $100 M_{\odot}$ and including the effects of stellar binaries. Using instead the relation of ref.³⁸, calibrated for lower redshift systems with close-to-solar metallicity, results in a higher SFR by a factor of ~ 2.5 . This difference is mainly attributed to the absence of low-metallicity stars and binary star interactions that produce higher ionization photons. In addition, we infer the SFR from the SED modelling as described below.

The $H\alpha$ line luminosity was also used to estimate the ionizing photon production efficiency, ξ_{ion} , following ref.⁵⁶, which is related to the number of produced ionizing photons per UV luminosity (or SFR). To be conservative, during this calculation we assume an escape fraction of $f_{\text{esc}} = 0$ (any other value above zero will result in a higher ξ_{ion}) and a dust attenuation of $A(V) = 0.3$ mag (note that the attenuation of the young stellar population inferred from our fiducial SED modelling is $A(V) = 0.1$ mag, with other models suggesting even lower values). Under these assumptions, we estimate an ionizing photon production efficiency of GHZ2 to be $\xi_{\text{ion}} \gtrsim 2 \times 10^{25} \text{ Hz erg}^{-1}$, as shown in Extended Data Fig. 4.

¹(<https://www.stsci.edu/contents/news/jwst/2024/updates-to-miri-low-resolution-spectrometer-reference-files>)

	$H\beta^\dagger$	[OIII]4959Å	[OIII]5007Å	$H\alpha$	[SII]6717Å,6731Å	[OIII]88 μm^\ddagger
Line flux [erg/s/cm ²] $\times 10^{-18}$	< 2.0 OR 0.9 ± 0.2	1.6 ± 0.2	4.7 ± 0.5	2.5 ± 0.7	< 2.6	< 0.25

Table 1: Measured line flux densities or upper limits without correcting for the potential effect of gravitational amplification ($\mu \approx 1.3$ according to ref. ¹³).

[†]Two values are given: a 2.5σ upper limit directly constrained from the data, and the inferred value from $H\alpha$ (valid in the case of zero dust attenuation; see text for details).

[‡] Scaled from ref. ⁴⁸ assuming a FWHM = 200 km/s.

5 Gravitational lensing modelling

A detailed strong-lensing model of the galaxy cluster Abell 2744 predicted ¹³ a gravitational amplification of $\mu = 1.3$ for GHZ2/GLASS-z12. Nevertheless, the presence of other bright galaxies along the line-of-sight (between the cluster and the target) might produce second-order effects. To test this, we modeled the total mass distribution of the closest galaxies as foreground lenses with one-component models, namely Singular Isothermal Sphere (SIS) profiles. Their redshifts and stellar masses were extracted from the GLASS catalog ⁵⁷, spanning $z \sim 1.5 - 3.5$ and $M_\star = 8 \times 10^7 - 2 \times 10^9 M_\odot$. The closest source is the most massive galaxy, with a spectroscopic redshift of $z = 1.682$. We assume a conservative effective velocity dispersion value of 100 km/s for all the galaxies, corresponding to the highest expected value given their stellar masses ⁵⁸. This was then used to estimate the associated Einstein angle for a source at the redshift of GHZ2 ($z = 12.33$). Finally, to assess the potential effect of this secondary gravitational lensing amplification, this angle was compared with the angular separation between the corresponding perturber mass center (after correcting its position for the deflection of the lens cluster) and the position of GHZ2/GLASS-z12 on the perturber’s plane.

Based on this analysis, we found that the angular separation between GHZ2 and the closest galaxy on its plane exceeds by more than five times ($\theta/\theta_E \approx 5.4$) the estimated Einstein angle (being 8-20x larger for the other foreground galaxies). While a simple SIS gravitational lens model would imply a magnification of $(1 - 1/5.4)^{-1} \approx 1.23$ from this close galaxy, the total magnification experienced by GHZ2 cannot simply be obtained by multiplying the magnification factor of the cluster by that of the galaxy (which would result in $\mu \approx 1.6$). This can only be accurately quantified using a multiplane lensing approach which is beyond the scope of this paper. Therefore, to avoid introducing biases relative to this modelling, we decided to adopt the value of ¹³ $\mu = 1.3$, but notice that the uncertainties on this value allows for slightly larger magnification values with increments in the order of $\sim 20 - 30\%$.

6 SED fitting

The broad-band spectral energy distribution, jointly with the spectroscopic measurements of the $H\alpha$ and [OIII] emission lines, were fitted to stellar population and nebular gas emission models to estimate the stellar mass, SFR, and mass-weighted age of GHZ2. The NIRCam photometry is slightly different from previous estimations ⁸ since we include new observations obtained in July 2023 (see ref. ¹¹ and Merlin et al. in prep. for further details). We used the SYNTHESIZER-AGN code ⁵⁹⁻⁶¹, with the stellar populations models from ref. ⁶² and with a Chabrier ⁶³ initial mass function with stellar mass limits between 0.1 and 100 M_\odot . We probed all sub-solar metallicity models. The star formation history was set to a double burst, each stellar population described by a delayed-exponential law with possible timescales ranging from 1 to 100 Myr, ages from 0.1 Myr to the age of the Universe at $z = 12.36$. Each stellar population is allowed to be affected by independent dust attenuations described by Calzetti law ⁵³, with A_V values ranging from 0 to 1 mag. Nebular continuum and line emission was modeled with CLOUDY version c23.0.1 ^{64,65}, assuming 10,000 K gas with 10^4 cm^{-3} density and abundances linked to the stellar metallicity and ionizing photon flux provided by the stellar models. The main derived properties (without correcting for the gravitational amplification) are: stellar mass $\log M_\star/M_\odot = 9.03^{+0.13}_{-0.28}$, $\text{SFR}_{10\text{Myr}} = 7 \pm 2 M_\odot \text{ yr}^{-1}$, mass-weighted age 28^{+10}_{-14} Myr. The models also support the high ionization parameter inferred from the BPT diagram, with a best-fit value of $\log U = -1.1 \pm 0.4$, and a consistent stellar metallicity of $Z/Z_\odot = 0.020^{+0.030}_{-0.015}$. The attenuation for older and younger star populations is constrained to be $A(V) = 0.3^{+0.1}_{-0.2}$ mag and $0.1^{+0.2}_{-0.1}$ mag, respectively. The best-fit SED obtained from this analysis is presented in the Supplementary information.

Additionally, we use the BAGPIPES ⁶⁶ and CIGALE ⁶⁷ SED-fitting codes with the same stellar population models, IMF, and dust attenuation law. In the case of BAGPIPES we adopt a “bursty continuity” model for the star formation history and found a general good agreement in the age of the stellar population (30^{+40}_{-20} Myr) with a very similar fraction of mass formed during the last 30 Myr.

Other parameters are also consistent within the error bars ($\log U = -1.4^{+0.2}_{-0.3}$; $\text{SFR} = 2^{+3}_{-1} \text{ M}_\odot \text{ yr}^{-1}$; $\log M_\star / \text{M}_\odot = 8.38^{+0.23}_{-0.18}$), with the major difference being the close-to-zero attenuation ($A(V) = 0.01^{+0.02}_{-0.01} \text{ mag}$) and a slightly higher metallicity ($Z = 0.22^{+0.06}_{-0.05} Z_\odot$). Similarly, the results with CIGALE implies a mass-weighted stellar age of $26 \pm 55 \text{ Myr}$, $\log M_\star / \text{M}_\odot = 8.3 \pm 0.3$, $\log U = -2.1 \pm 0.5$, $A(V) = 0.11^{+0.13}_{-0.11} \text{ mag}$, and $\text{SFR}_{10\text{Myr}} = 15 \pm 9 \text{ M}_\odot \text{ yr}^{-1}$, with an even higher (but largely uncertain) metallicity of $Z = 0.56 \pm 0.20 Z_\odot$. Note that all these values are not corrected for gravitational amplification.

7 Photoionization and line emissivity models

The photoionization models presented in Fig. 2, showing the ratio between [OIII]5007Å and H β and between [NII]6583Å and H α , are taken from ref.²⁰. They were calculated using the spectral synthesis code, CLOUDY⁶⁸, and assuming the stellar population models from BPASS, including binaries systems, with a Kroupa IMF with an upper mass cut of 300 M_\odot (although similar results are obtained for $M_{\text{up}} = 100 \text{ M}_\odot$). In these models, the ionization parameter, defined as the ratio between the hydrogen-ionizing photons and the number density of hydrogen atoms, was varied from -3.5 to -1.0, while the gas electron density was fixed to 10^3 cm^{-3} . As seen in Fig. 2, the [OIII]5007Å-to-H β line ratio of GHZ2 is reproduced only by models with high ionization parameter above -2.0 (in the case of $Z \approx 0.1 - 0.2 Z_\odot$). At lower metallicities ($Z \lesssim 0.05 Z_\odot$), the models predictions lie below the inferred value and would require harder ionizing radiation to explain the observational constraints. For instance, AGN-driven models show higher [OIII]5007Å-to-H β ratios (by $\sim 0.3 \text{ dex}$), when compared with the stellar-driven models at fixed metallicity²⁰.

On the other hand, the predicted line ratios between the two transitions of the double-ionized oxygen ([OIII]5007Å and [OIII]88 μm) shown in Fig. 3 were generated using the PyNeb getEmissivity package⁶⁹, with the default atomic data. The ratio was calculated for different values of electron density and temperature ranging from $\log(n_e [\text{cm}^{-3}]) = 0 - 10$ and $\log(T_e [\text{K}]) = 3.7 - 4.5$. As can be seen in the figure, the ratio is highly sensitive to electron density with a milder dependency on electron temperature (given the significant different energy levels of the two transitions), but independent of metallicity since both transitions arise from the same ion.

8 Revisiting the ALMA data and constraining the electron density

The initial investigation of GHZ2/GLASS-z12 at sub-mm wavelengths with ALMA only revealed a tentative line⁴⁸

at 258.7 GHz, claimed to be [OIII]88 μm at $z = 12.117$. This is inconsistent with the MIRI and NIRSpectroscopic redshift, implying that the line was not real or, at least, not associated with GHZ2. With the updated redshift information, we visually inspect the 254.35 GHz region and fit the extracted spectrum using a single Gaussian function, centered at the peak channel. The best-fit implies a line flux of $\sim 2.5 \times 10^{-19} \text{ erg/s/cm}^{-2}$ with $\text{FWHM} \approx 200 \text{ km s}^{-1}$, which is consistent with the previously reported^{48,70} upper limit, after taking into account the different line-widths (originally adopted to be $\approx 100 \text{ km s}^{-1}$ in the previous ALMA analysis⁴⁸). Given the low statistical significance ($\sim 3\sigma$) of this measurement, to be conservative, we treat it here only as an upper limit. This implies a [OIII]5007Å-to-[OIII]88 μm line ratio above 19 (or $\log([\text{OIII}]_{5007\text{Å}} / [\text{OIII}]_{88\mu\text{m}}) \gtrsim 1.3$) and is used in Fig. 3 to obtain a conservative lower limit on the electron density of $n_e > 100 \text{ cm}^{-3}$, which varies as a function of electron temperature. Assuming the typical value of $T_e = 10,000 \text{ K}$, the current constraints imply an extreme n_e value above $1,000 \text{ cm}^{-3}$. This is consistent with the picture of higher electron densities at high redshifts, as shown in Extended Data Fig. 5.

High electron densities would naturally explain other non-detections of the [OIII]88 μm line⁷¹ at $z > 10$ given its relatively low critical density of²⁶ $n_c \approx 5 \times 10^2 \text{ cm}^{-3}$. Above this value, collisional deexcitation plays a significant role in gas cooling, diminishing the line luminosity produced by radiative cooling that is more efficient in the low density regime. Hence, future ALMA follow-up may be more successful by targeting the [OIII]52 μm line thanks to its higher critical density of $n_c \approx 3 \times 10^3 \text{ cm}^{-3}$.

References

1. Arrabal Haro, P. *et al.* Confirmation and refutation of very luminous galaxies in the early Universe. *Nature* **622**, 707–711 (2023).
2. Bunker, A. J. *et al.* JADES NIRSpec Spectroscopy of GN-z11: Lyman- α emission and possible enhanced nitrogen abundance in a $z = 10.60$ luminous galaxy. *Astron. Astrophys.* **677**, A88 (2023).
3. Harikane, Y. *et al.* Pure Spectroscopic Constraints on UV Luminosity Functions and Cosmic Star Formation History from 25 Galaxies at $z_{\text{spec}} = 8.61\text{--}13.20$ Confirmed with JWST/NIRSpec. *Astrophys. J.* **960**, 56 (2024).
4. Trump, J. R. *et al.* The Physical Conditions of Emission-line Galaxies at Cosmic Dawn from JWST/NIRSpec Spectroscopy in the SMACS 0723 Early Release Observations. *Astrophys. J.* **945**, 35 (2023).
5. Sanders, R. L., Shapley, A. E., Topping, M. W., Reddy, N. A. & Brammer, G. B. Excitation and Ionization Properties of Star-forming Galaxies at $z = 2.0\text{--}9.3$ with JWST/NIRSpec. *Astrophys. J.* **955**, 54 (2023).
6. Rieke, G. H. *et al.* The Mid-Infrared Instrument for the James Webb Space Telescope, I: Introduction. *PASP* **127**, 584 (2015).
7. Rigby, J. *et al.* The Science Performance of JWST as Characterized in Commissioning. *PASP* **135**, 048001 (2023).
8. Castellano, M. *et al.* Early Results from GLASS-JWST. III. Galaxy Candidates at $z = 9\text{--}15$. *Astrophys. J. Lett.* **938**, L15 (2022).
9. Naidu, R. P. *et al.* Two Remarkably Luminous Galaxy Candidates at $z \approx 10\text{--}12$ Revealed by JWST. *Astrophys. J. Lett.* **940**, L14 (2022).
10. Treu, T. *et al.* The GLASS-JWST Early Release Science Program. I. Survey Design and Release Plans. *Astrophys. J.* **935**, 110 (2022).
11. Castellano, M. *et al.* JWST NIRSpec Spectroscopy of the Remarkable Bright Galaxy GHZ2/GLASS-z12 at Redshift 12.34. *arXiv e-prints* arXiv:2403.10238 (2024).
12. Ono, Y. *et al.* Morphologies of Galaxies at $z \gtrsim 9$ Uncovered by JWST/NIRCam Imaging: Cosmic Size Evolution and an Identification of an Extremely Compact Bright Galaxy at $z = 12$. *Astrophys. J.* **951**, 72 (2023).
13. Bergamini, P. *et al.* The GLASS-JWST Early Release Science Program. III. Strong-lensing Model of Abell 2744 and Its Infalling Regions. *Astrophys. J.* **952**, 84 (2023).
14. Curtis-Lake, E. *et al.* Spectroscopic confirmation of four metal-poor galaxies at $z = 10.3\text{--}13.2$. *Nature Astronomy* **7**, 622–632 (2023).
15. D'Eugenio, F. *et al.* JADES: Carbon enrichment 350 Myr after the Big Bang in a gas-rich galaxy. *arXiv e-prints* arXiv:2311.09908 (2023).
16. Wang, B. *et al.* UNCOVER: Illuminating the Early Universe—JWST/NIRSpec Confirmation of $z \lesssim 12$ Galaxies. *Astrophys. J. Lett.* **957**, L34 (2023).
17. Carniani, S. *et al.* A shining cosmic dawn: spectroscopic confirmation of two luminous galaxies at $z \sim 14$. *arXiv e-prints* arXiv:2405.18485 (2024).
18. Storey, P. J. & Zeippen, C. J. Theoretical values for the [OIII] 5007/4959 line-intensity ratio and homologous cases. *Mon. Not. R. Astron. Soc.* **312**, 813–816 (2000).
19. Groves, B. A., Heckman, T. M. & Kauffmann, G. Emission-line diagnostics of low-metallicity active galactic nuclei. *Mon. Not. R. Astron. Soc.* **371**, 1559–1569 (2006).
20. Nakajima, K. & Maiolino, R. Diagnostics for PopIII galaxies and direct collapse black holes in the early universe. *Mon. Not. R. Astron. Soc.* **513**, 5134–5147 (2022).
21. Cameron, A. J. *et al.* JADES: Probing interstellar medium conditions at $z \sim 5.5\text{--}9.5$ with ultra-deep JWST/NIRSpec spectroscopy. *Astron. Astrophys.* **677**, A115 (2023).
22. Calabrò, A. *et al.* The evolution of the SFR and Σ_{SFR} of galaxies in cosmic morning ($4 < z < 10$). *arXiv e-prints* arXiv:2402.17829 (2024).
23. Topping, M. W. *et al.* Metal-poor star formation at $z > 6$ with JWST: new insight into hard radiation fields and nitrogen enrichment on 20 pc scales. *arXiv e-prints* arXiv:2401.08764 (2024).
24. Kocevski, D. D. *et al.* Hidden Little Monsters: Spectroscopic Identification of Low-mass, Broad-line AGNs at $z \lesssim 5$ with CEERS. *Astrophys. J. Lett.* **954**, L4 (2023).
25. Harikane, Y. *et al.* A JWST/NIRSpec First Census of Broad-line AGNs at $z = 4\text{--}7$: Detection of 10 Faint AGNs with $M_{\text{BH}} 10^6\text{--}10^8 M_{\odot}$ and Their Host Galaxy Properties. *Astrophys. J.* **959**, 39 (2023).
26. Osterbrock, D. E. & Ferland, G. J. *Astrophysics of gaseous nebulae and active galactic nuclei* (2006).
27. Nakajima, K. *et al.* JWST Census for the Mass-Metallicity Star Formation Relations at $z = 4\text{--}10$ with Self-consistent Flux Calibration and Proper Metallicity Calibrators. *Astrophys. J. Suppl.* **269**, 33 (2023).
28. Ma, X. *et al.* The origin and evolution of the galaxy mass-metallicity relation. *Mon. Not. R. Astron. Soc.* **456**, 2140–2156 (2016).
29. Ucci, G. *et al.* Astraeus V: the emergence and evolution of metallicity scaling relations during the epoch of reionization. *Mon. Not. R. Astron. Soc.* **518**, 3557–3575 (2023).
30. Torrey, P. *et al.* The evolution of the mass-metallicity relation and its scatter in IllustrisTNG. *Mon. Not. R. Astron. Soc.* **484**, 5587–5607 (2019).
31. Endsley, R. *et al.* The Star-forming and Ionizing Properties of Dwarf $z\text{--}6\text{--}9$ Galaxies in JADES: Insights on Bursty Star Formation and Ionized Bubble Growth. *arXiv e-prints* arXiv:2306.05295 (2023).

32. Ciesla, L. *et al.* Identification of a transition from stochastic to secular star formation around $z = 9$ with JWST. *arXiv e-prints* arXiv:2309.15720 (2023).
33. Tacchella, S. *et al.* On the Stellar Populations of Galaxies at $z = 9$ –11: The Growth of Metals and Stellar Mass at Early Times. *Astrophys. J.* **927**, 170 (2022).
34. Cole, J. W. *et al.* CEERS: Increasing Scatter along the Star-Forming Main Sequence Indicates Early Galaxies Form in Bursts. *arXiv e-prints* arXiv:2312.10152 (2023).
35. Finkelstein, S. L. *et al.* The Complete CEERS Early Universe Galaxy Sample: A Surprisingly Slow Evolution of the Space Density of Bright Galaxies at $z \sim 8.5$ –14.5. *arXiv e-prints* arXiv:2311.04279 (2023).
36. Adams, N. J. *et al.* EPOCHS Paper II: The Ultraviolet Luminosity Function from $7.5 < z < 13.5$ using 180 square arcminutes of deep, blank-fields from the PEARLS Survey and Public JWST data. *arXiv e-prints* arXiv:2304.13721 (2023).
37. Reddy, N. A. *et al.* The Effects of Stellar Population and Gas Covering Fraction on the Emergent Ly α Emission of High-redshift Galaxies. *Astrophys. J.* **926**, 31 (2022).
38. Kennicutt, R. C. & Evans, N. J. Star Formation in the Milky Way and Nearby Galaxies. *Annual Review of Astronomy and Astrophysics* **50**, 531–608 (2012).
39. Nagao, T., Maiolino, R. & Marconi, A. Gas metallicity diagnostics in star-forming galaxies. *Astron. Astrophys.* **459**, 85–101 (2006).
40. Sanders, R. L., Shapley, A. E., Topping, M. W., Reddy, N. A. & Brammer, G. B. Direct T_e -based Metallicities of $z = 2$ –9 Galaxies with JWST/NIRSpec: Empirical Metallicity Calibrations Applicable from Reionization to Cosmic Noon. *Astrophys. J.* **962**, 24 (2024).
41. Hirschmann, M., Charlot, S. & Somerville, R. S. High-redshift metallicity calibrations for JWST spectra: insights from line emission in cosmological simulations. *Mon. Not. R. Astron. Soc.* **526**, 3504–3518 (2023).
42. Curti, M., Mannucci, F., Cresci, G. & Maiolino, R. The mass-metallicity and the fundamental metallicity relation revisited on a fully T_e -based abundance scale for galaxies. *Mon. Not. R. Astron. Soc.* **491**, 944–964 (2020).
43. Kaasinen, M., Bian, F., Groves, B., Kewley, L. J. & Gupta, A. The COSMOS-[O II] survey: evolution of electron density with star formation rate. *Mon. Not. R. Astron. Soc.* **465**, 3220–3234 (2017).
44. Nakajima, K. *et al.* EMPRESS. V. Metallicity Diagnostics of Galaxies over $12 + \log(\text{O}/\text{H}) = 6.9$ –8.9 Established by a Local Galaxy Census: Preparing for JWST Spectroscopy. *Astrophys. J. Suppl.* **262**, 3 (2022).
45. Schaerer, D., Fragos, T. & Izotov, Y. I. X-ray binaries as the origin of nebular He II emission in low-metallicity star-forming galaxies. *Astron. Astrophys.* **622**, L10 (2019).
46. Lecroq, M. *et al.* Nebular emission from young stellar populations including binary stars. *Mon. Not. R. Astron. Soc.* **527**, 9480–9504 (2024).
47. Upadhyaya, A. *et al.* Evidence for Very Massive Stars in extremely UV-bright star-forming galaxies at $z \sim 2.2$ –3.6. *arXiv e-prints* arXiv:2401.16165 (2024).
48. Bakx, T. J. L. C. *et al.* Deep ALMA redshift search of a $z \sim 12$ GLASS-JWST galaxy candidate. *Mon. Not. R. Astron. Soc.* **519**, 5076–5085 (2023).
49. Isobe, Y. *et al.* Redshift Evolution of Electron Density in the Interstellar Medium at $z \sim 0$ –9 Uncovered with JWST/NIRSpec Spectra and Line-spread Function Determinations. *Astrophys. J.* **956**, 139 (2023).
50. Reddy, N. A., Topping, M. W., Sanders, R. L., Shapley, A. E. & Brammer, G. A JWST/NIRSpec Exploration of the Connection between Ionization Parameter, Electron Density, and Star-formation-rate Surface Density in $z = 2.7$ –6.3 Galaxies. *Astrophys. J.* **952**, 167 (2023).
51. Asplund, M., Grevesse, N., Sauval, A. J. & Scott, P. The Chemical Composition of the Sun. *Annual Review of Astronomy and Astrophysics* **47**, 481–522 (2009).
52. Kendrew, S. *et al.* The Mid-Infrared Instrument for the James Webb Space Telescope, IV: The Low-Resolution Spectrometer. *PASP* **127**, 623 (2015).
53. Calzetti, D. *et al.* The Dust Content and Opacity of Actively Star-forming Galaxies. *Astrophys. J.* **533**, 682–695 (2000).
54. Beiler, S. A. *et al.* The First JWST Spectral Energy Distribution of a Y Dwarf. *Astrophys. J. Lett.* **951**, L48 (2023).
55. Pillepich, A. *et al.* Simulating galaxy formation with the IllustrisTNG model. *Mon. Not. R. Astron. Soc.* **473**, 4077–4106 (2018).
56. Matthee, J. *et al.* The production and escape of Lyman-Continuum radiation from star-forming galaxies at $z \sim 2$ and their redshift evolution. *Mon. Not. R. Astron. Soc.* **465**, 3637–3655 (2017).
57. Paris, D. *et al.* The GLASS-JWST Early Release Science Program. II. Stage I Release of NIRCIm Imaging and Catalogs in the Abell 2744 Region. *Astrophys. J.* **952**, 20 (2023).
58. Grillo, C. *et al.* CLASH: Extending Galaxy Strong Lensing to Small Physical Scales with Distant Sources Highly Magnified by Galaxy Cluster Members. *Astrophys. J.* **786**, 11 (2014).
59. Pérez-González, P. G. *et al.* Stellar populations in local star-forming galaxies - I. Data and modelling procedure. *Mon. Not. R. Astron. Soc.* **338**, 508–524 (2003).
60. Pérez-González, P. G. *et al.* The Stellar Mass Assembly of Galaxies from $z = 0$ to $z = 4$: Analysis of a Sample Selected in the Rest-Frame Near-Infrared with Spitzer. *Astrophys. J.* **675**, 234–261 (2008).

61. Pérez-González, P. G. *et al.* What is the nature of Little Red Dots and what is not, MIRI SMILES edition. *arXiv e-prints* arXiv:2401.08782 (2024).
62. Bruzual, G. & Charlot, S. Stellar population synthesis at the resolution of 2003. *Mon. Not. R. Astron. Soc.* **344**, 1000–1028 (2003).
63. Chabrier, G. Galactic Stellar and Substellar Initial Mass Function. *PASP* **115**, 763–795 (2003).
64. Ferland, G. J. *et al.* CLOUDY 90: Numerical Simulation of Plasmas and Their Spectra. *PASP* **110**, 761–778 (1998).
65. Chatzikos, M. *et al.* The 2023 Release of Cloudy. *Rev. Mexic. Astron. Astrof.* **59**, 327–343 (2023).
66. Carnall, A. C., McLure, R. J., Dunlop, J. S. & Davé, R. Inferring the star formation histories of massive quiescent galaxies with BAGPIPES: evidence for multiple quenching mechanisms. *Mon. Not. R. Astron. Soc.* **480**, 4379–4401 (2018).
67. Boquien, M. *et al.* CIGALE: a python Code Investigating GALaxy Emission. *Astron. Astrophys.* **622**, A103 (2019).
68. Ferland, G. J. *et al.* The 2017 Release Cloudy. *Rev. Mexic. Astron. Astrof.* **53**, 385–438 (2017).
69. Luridiana, V., Morisset, C. & Shaw, R. A. PyNeb: a new tool for analyzing emission lines. I. Code description and validation of results. *Astron. Astrophys.* **573**, A42 (2015).
70. Popping, G. An upper limit on [O III] 88 μ m and 1.2 mm continuum emission from a JWST $z \approx 12$ -13 galaxy candidate with ALMA. *Astron. Astrophys.* **669**, L8 (2023).
71. Yoon, I. *et al.* ALMA Observation of a $z \gtrsim 10$ Galaxy Candidate Discovered with JWST. *Astrophys. J.* **950**, 61 (2023).
72. Matthee, J. *et al.* EIGER. II. First Spectroscopic Characterization of the Young Stars and Ionized Gas Associated with Strong H β and [O III] Line Emission in Galaxies at $z = 5$ -7 with JWST. *Astrophys. J.* **950**, 67 (2023).
73. Rinaldi, P. *et al.* MIDIS: Unveiling the Role of Strong H α emitters during the Epoch of Reionization with JWST. *arXiv e-prints* arXiv:2309.15671 (2023).
74. Álvarez-Márquez, J. *et al.* Spatially resolved H α and ionizing photon production efficiency in the lensed galaxy MACS1149-JD1 at a redshift of 9.11. *Astron. Astrophys.* **686**, A85 (2024).
75. Atek, H. *et al.* Most of the photons that reionized the Universe came from dwarf galaxies. *Nature* **626**, 975–978 (2024).
76. Fujimoto, S. *et al.* CEERS Spectroscopic Confirmation of NIRC2-selected $z \gtrsim 8$ Galaxy Candidates with JWST/NIRSpec: Initial Characterization of Their Properties. *Astrophys. J. Lett.* **949**, L25 (2023).
77. Hsiao, T. Y.-Y. *et al.* JWST MIRI detections of H α and [O III] and direct metallicity measurement of the $z = 10.17$ lensed galaxy MACS0647-JD. *arXiv e-prints* arXiv:2404.16200 (2024).
78. Lin, Y.-H. *et al.* An empirical reionization history model inferred from the low-redshift Lyman continuum survey and the star-forming galaxies at $z \lesssim 8$. *Mon. Not. R. Astron. Soc.* **527**, 4173–4182 (2024).
79. Stark, D. P. *et al.* Spectroscopic detection of C IV $\lambda 1548$ in a galaxy at $z = 7.045$: implications for the ionizing spectra of reionization-era galaxies. *Mon. Not. R. Astron. Soc.* **454**, 1393–1403 (2015).
80. Stark, D. P. *et al.* Ly α and C III] emission in $z = 7$ -9 Galaxies: accelerated reionization around luminous star-forming systems? *Mon. Not. R. Astron. Soc.* **464**, 469–479 (2017).
81. Robertson, B. E. *et al.* New Constraints on Cosmic Reionization from the 2012 Hubble Ultra Deep Field Campaign. *Astrophys. J.* **768**, 71 (2013).
82. Fujimoto, S. *et al.* JWST and ALMA Multiple-line Study in and around a Galaxy at $z = 8.496$: Optical to Far-Infrared Line Ratios and the Onset of an Outflow Promoting Ionizing Photon Escape. *Astrophys. J.* **964**, 146 (2024).

Extended Data Figures

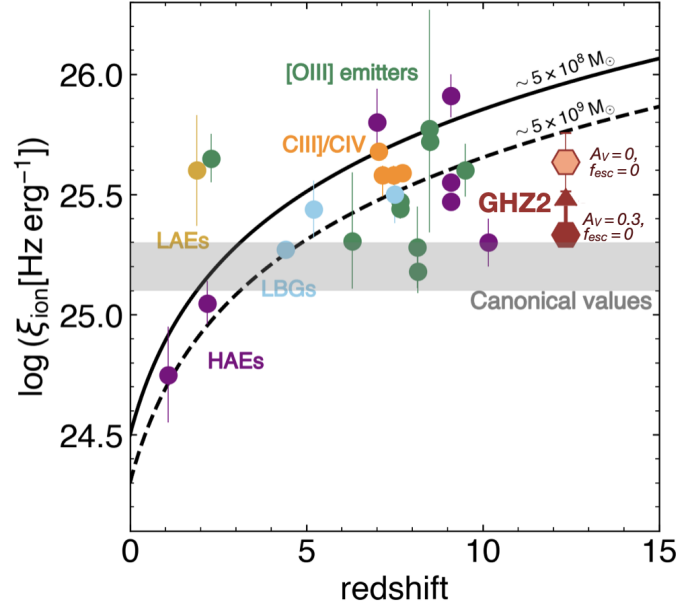


Figure 4: **Ionizing photon production efficiency.** Inferred ionizing photon production efficiency for GHZ2 assuming a conservative dust attenuation of $A(V) = 0.3$ mag (illustrated with the solid hexagon). For comparison, we show the inferred value for a zero dust attenuation (light red) and estimated values for other samples (average values⁷² and individual measurements^{73–80}), along with the redshift evolution from ref.⁵⁶. Error bars represent 1σ errors in the case of individual measurements or the scatter of the measurements for samples' average. The bright $H\alpha$ emission of GHZ2 implies a high ionizing photon production, likely above the typical values adopted for galaxies contributing to the reionization process⁸¹.

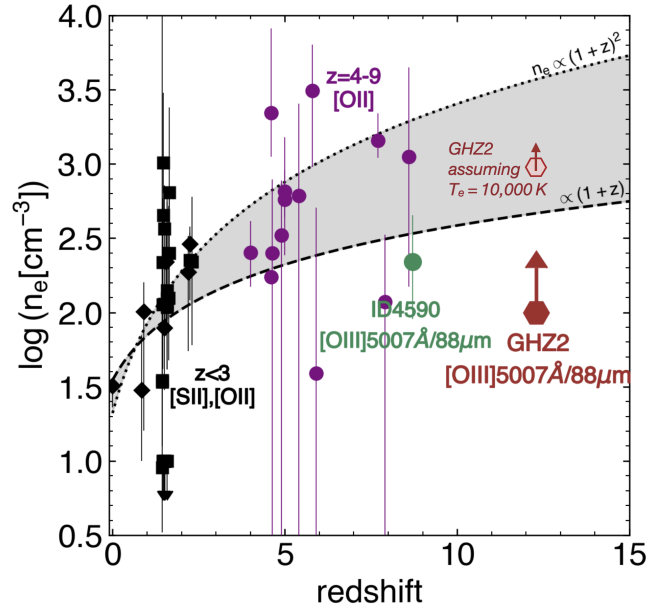


Figure 5: **The redshift evolution of the electron density.** Compilation of spectroscopically-derived measurements (with 1σ error bars) of ionized gas electron density in galaxies at different redshifts (modified from ref.⁴⁹ and including other measurements^{43,82}) along with the constraints inferred for our target, GHZ2, at $z = 12.33$. Our results support the evolution towards higher electron densities at high redshifts, which might be associated with the high ionization parameters and high star formation rate surface densities of the bright population of high-redshift galaxies recently discovered with JWST.

Supplementary Information

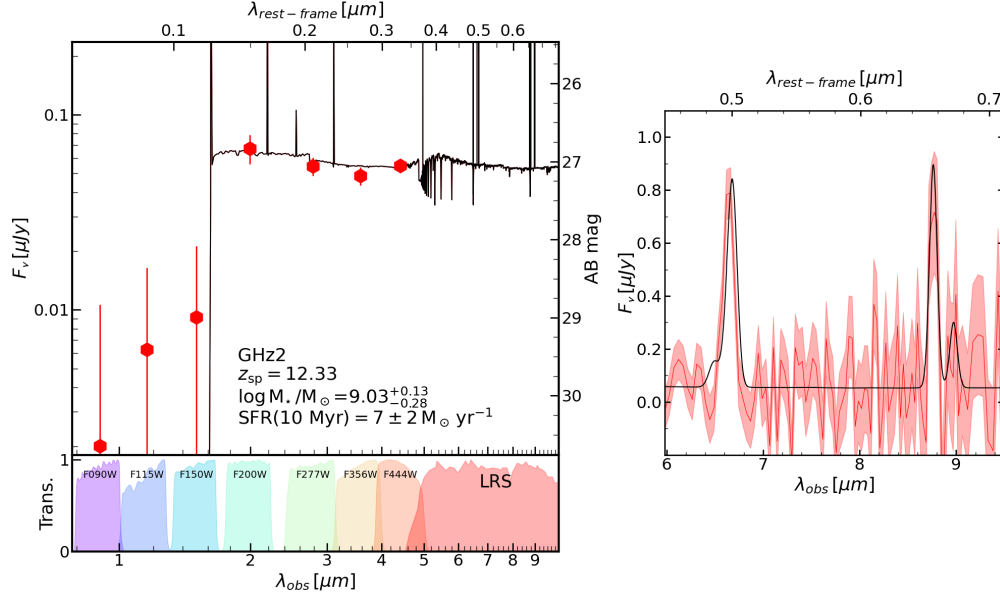


Figure 6: **The best-fit spectral Energy Distribution of GHZ2/GLASS-z12.** Example of our photo-spectroscopic analysis combining the NIRCам photometry (illustrated by the red points on the left panel with associated 1σ uncertainties) and the MIRI/LRS spectra (illustrated by the red solid line on the right panel and shaded region showing 1σ uncertainties). The best-fit SED obtained with the SYNTHESIZER code is shown by the black solid line (original spectral resolution on the left panel, convolved to the resolution of MIRI/LRS on the right panel) along with some of the best-fit parameters (without correcting for gravitational amplification). Note that CIGALE and SYNTHESIZER only use the line fluxes information in the fitting (along with the measured photometry), while BAGPIPES uses the full spectrum as an input.